ORIGINAL PAPER

Numerical research on near stall characteristics of a transonic axial compressor based on wavelet analysis

Kailong Xia[1] · Mingmin Zhu[1] · Junda Feng[2] · Hefang Deng[1] · Xiaoqing Qiang[1] · Jinfang Teng[1]

Abstract

An axial single-stage high-speed test rig is numerically studied in this paper with half-annulus URANS simulations to describe the flow characteristics at the near stall condition. Wavelet analysis is applied to demonstrate the time–frequency characteristics of the near-tip pressure signals captured by the numerical probes at different circumferential and axial positions. The detailed tip flow fields and wavelet transform results are combined to depict the generation and propagation of the spike-type stall inception. According to the wavelet spectrum, characteristic frequencies correspond to the temporal and spatial features of the rotating stall, such as the fluctuation of the shock wave, self-oscillation and propagation of tip leakage vortex et al. Consequently, the detection of typical spike stall inception can be significantly brought forward by identifying the crucial rotating disturbance and its development for the onset of stall inception. Then, the specific tip flow fields are also discussed to reveal the flow mechanism of stall inception evolution, including the leading edge spillage and the trailing edge backflow. Further investigation shows that the stall inception with smooth casing corresponds to the radial separation vortex caused by the tip leading edge spillage, which continues to develop and propagate in the circumferential direction and finally induces the stall.

Keywords Axial transonic compressor · Unsteady simulation · Tip leakage flow · Stall inception · Wavelet analysis

Abbreviations

DSFT	Discrete spatial Fourier transform
DTC	Darmstadt transonic compressor
EMD	Empirical mode decomposition
HHT	Hilbert-Huang transform
ILU	Incomplete lower upper
LE	Leading edge
NS	Near stall
PE	Peak efficiency
PS	Pressure surface
RANS	Reynolds average Navier–stokes
SS	Suction surface
SST	Shear stress transport
STFT	Short time Fourier transform
TE	Trailing edge
URANS	Unsteady Reynolds average Navier–Stokes

List of symbols

C_{ax}	Axial chord length
η^*	Isentropic efficiency
N	Rotating speed
π^*	Total pressure ratio
T	Rotating period of the DTC rotor
ω_0	Central frequency

✉ Mingmin Zhu
jackzhushen@sjtu.edu.cn

1 School of Aeronautics and Astronautics, Shanghai Jiao Tong University, Shanghai, China

2 AECC Commercial Aircraft Engine Co., Ltd, Shanghai, China

1 Introduction

It has been widely acknowledged over the past 80 years that there are two well-established types of a stall, referred to as "modal" inception with large length-scale and "spike" inception with small one [1]. Owing to the features of three-dimensionality, nonlinearity and short time duration, it is undoubtedly detrimental to detect the pre-stall warning signal

of spike inception, which makes the capture and identification of its signal information become the recent interest [2].

Many efforts have been expended over recent decades to fundamentally comprehend these disturbances' mechanisms. An experimental investigation of stall inception and stall cell development in a single-stage axial compressor was conducted in 1986 by Whittle Laboratory [3]. The stall cell was first observed behind the rotor at a small distance from the tip, which proliferated and propagated circumferentially. McDougall et al. [4] made a detailed measurement of the transient stalling process and suggested that tip stalling is more likely at the level of clearance typical of multistage compressors. Camp and Day [5] proposed a simple model to indicate the occurrence of stalling patterns based on the critical rotor incidence. Specifically speaking, if the peak of the overall characteristics is reached before the critical value of rotor incidence is exceeded anywhere in the compressor, then modal-type inception will occur. In another case, spikes will appear in the overloaded rotor.

Developments in computing techniques helped researchers to use numerical methods to further investigate the mechanisms of stall inception. Vo et al. [6] drew attention to the necessary conditions for forming spike disturbances derived from multi-passage simulation, and what they hypothesized has been extensively verified in subsequent studies. One is that the interface between the tip clearance and oncoming flows becomes parallel to the leading edge (LE) plane. The second is the initiation of backflow, stemming from the fluid in adjacent passages, at the trailing edge (TE) plane. It is worth noting that both conditions are linked to the tip clearance flow. However, the later study from Pullan et al. [7] demonstrated that separation causes spikes in the LE due to excessive incidence. They claimed that blade tip leakage flow is not necessary for the spike-type stall.

The spike stall has been experimentally identified as propagating low-pressure regions on the casing wall around the leading edge from the series of studies from Inoue et al. [8], they conducted that the "Tornado-shaped" vortex with the open end attached to the casing and another end terminated at the suction side (SS) of the blade causes the spike inception. Yamada et al. [9] performed a further study to describe the flow mechanism of the tornado-like vortex: it propagates circumferentially and progressively develops into multiple stall cells during moderate stall. Supported by experimental data, Smith et al. [10]'s unsteady simulations showed two competing mechanisms cause the high incidence responsible for the L separation: blockage from casing corner separation and forward spillage of tip leakage flow. Then, Kim et al. [11] conducted further research and interpretation of the theoretical model.

Dynamic pressure probes installed at rotor casing have often been used to depict the flow behaviors during the pre-stall and stall inception periods [12]. Various methods are proposed to analyze the unsteady casing pressure from circumferential arrays. McDougall et al. [4] first applied Discrete Spatial Fourier Transform (DSFT) to analyze stall inception data and observed the detailed flow characteristics of the modal wave. However, DSFT is inadequate for detecting spike-type disturbance due to the limitation of the sampling frequency [13]. Short-time Fourier Transform (STFT), as a typical time–frequency analysis method, decomposes unsteady signals into multiple stationary parts. Several attempts have been made [14, 15] to observe the occurrence and development of rotating stalls. Meanwhile, the wavelet transform was exploited as a priority for indicating flow characteristics and detecting stall inception on account of its time–frequency ability. The first systematic report on wavelet analysis was carried out by Morlet and Grossmann [16] in 1984. By disintegrating signals into elementary building blocks well localized in space and frequency, the wavelet transform can characterize the local regularity of signals. It is fully demonstrated from Lin's research [17] that proper use of wavelet transform can uncover the details of the behavior of the spikes, and the size, location, time of initiation, and evolution of the disturbance can be tracked. Since the choice of the wavelet base is crucial to the global analysis, plenty of research has been conducted to build a deeper comprehension of how to center frequency ω_0 affects the wavelet analysis result [17–19]. At the same time, the Hilbert-Huang Transform (HHT) with the empirical mode decomposition (EMD) method has also been thoroughly studied as a comparison for stalling research [20, 21]. Besides, wavelet coherence and corresponding correlation analysis technologies are subsequently applied to track the developments of rotating disturbances and stall inception by Zhang et al. [18, 22]. Adaptive learning and optimization algorithms have attracted extensive attention recently. A high-order distortion dynamic mode was derived to depict the stalling signals by Lin et al. [23]. It is innovative that the stall detection approach for axial compressors in this paper is proposed with non-uniform inflow by using the deterministic learning algorithm. According to previous research summarized above, it is practicable to capture the process of the generation and propagation of the spike-type stall inception through multiple time–frequency analysis skills.

In this paper, an axial single-stage high-speed compressor was numerically studied with half-annulus URANS simulations. Wavelet analysis was utilized to process the wall pressure signal collected by numerical probes arranged circumferentially at different axial positions. The detailed tip flow fields and time–frequency analysis on tip pressure signals at the near stall condition were combined to demonstrate the characteristics of stall inception. Simultaneously, the specific phenomena were further discussed to reveal the flow mechanism of stall inception evolution. The rest of the paper
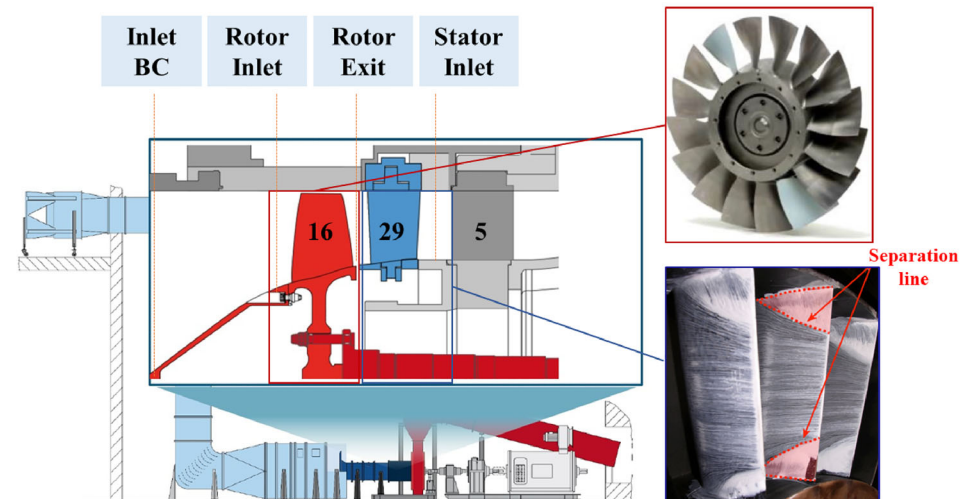
is organized as follows. The preliminary works of the simulation setting are introduced in Sect. 2. Section 3 shows the main results, including wavelet analysis and flow characteristics of the stall inception pattern. Section 4 gives the conclusions of this paper.

2 Methodology

2.1 Investigated compressor

The investigated compressor is the Darmstadt Transonic Compressor (DTC), an axial single-stage high-speed test rig at the Institute of Gas Turbines and Aerospace Propulsion, Technical University of Darmstadt. It was built in cooperation with MTU Aero Engines and went into service in 1994. As a typical design of a high-pressure compressor in a modern turbofan engine, the rotors of DTC are often used for developing new approaches to flow control and verification of numerical simulation results.

Figure 1 shows the cross-section of the single transonic compressor stage. It consists of a blisk rotor with 16 radially stacked CDA airfoils and a stator row with 29 blades of ordinary 2D design. It is characterized by a maximum pre-shock Mach number of 1.35 at a design speed of 20000 rpm. The design total pressure ratio of the inlet stage reaches 1.5 at the mass flow rate of 16.0 kg/s, while the tip clearance is approximately 1.7% span. Table 1 provides the crucial parameters of the blade at the design point [24].

2.2 Numerical procedure

The commercial three-dimensional Navier–Stokes flow solver, ANSYS-CFX, performs steady and unsteady simulations. To ensure the solver's robustness, CFX uses

Table 1 Design parameters of DTC [24]

Parameter (unit)	Value
Rotor/Stator number (–)	16/29
Rotating speed (RPM)	20,000
Design mass flow (kg/s)	16
Design total pressure ratio (–)	1.5
Tip diameter (m)	0.38
Rotor tip gap (% of span)	1.7
Rotor mean aspect ratio (–)	0.94
tip tangential speed (m/s)	398
Inlet Mach number at tip/hub (–)	1.35/0.7

the element-based finite volume method to discretize the Reynolds-Average Navier–Stokes equation based on unstructured grids. It utilizes an implicit coupled solver that solves all the hydrodynamic equations as a single system. The linearized equations are solved by the Incomplete Lower Upper (ILU) factorization technique, accelerated by an algebraic multigrid method. A pseudo-time-stepping algorithm with an automatic time scale technique is used for steady-state calculations. For the best practice of turbomachinery simulation, the Menter $k - \omega$ Shear Stress Transport (SST-2003) turbulence model [25], and the second-order accurate high-resolution advection scheme are recommended.

Figure 2 illustrates the 3D view of the simulation domain. In order to save computation resources, stators are removed from the simulation by excluding the downstream influence [26]. A single passage is calculated with the circumferential periodic boundary conditions. Inlet and outlet planes are applied as channel extensions by nine-times axial chords upstream and downstream of the rotor blade to avoid numerical reflection, respectively. Adiabatic and no-slip solid boundaries are applied at the hub, casing, and blade surfaces,

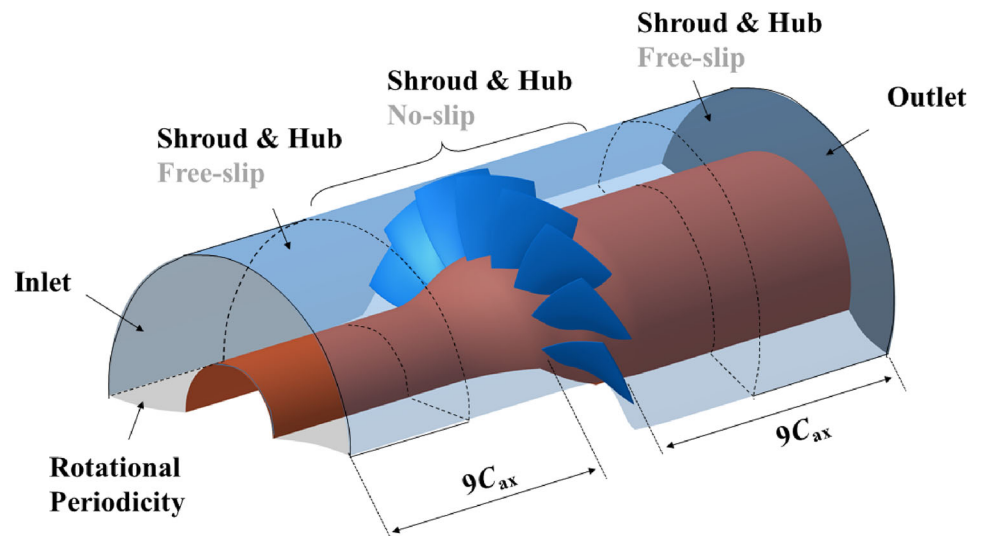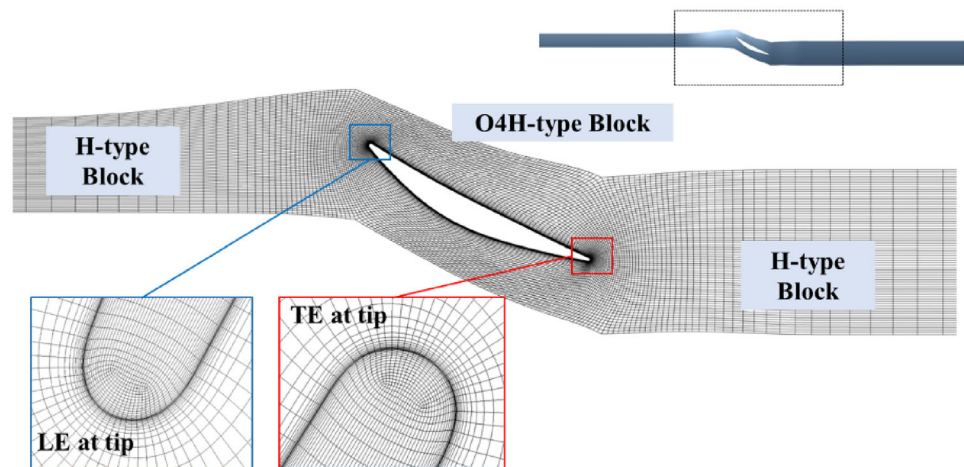**Fig. 2** Simulation domain and boundary conditions

Fig. 3 Illustration of the grid topology

while the free-sliding boundaries are adopted on the solid wall near the inlet and the outlet. A constant total pressure of 101,325 Pa and a total temperature of 288 K are applied. Static pressure is imposed at the outlet to vary the operating points for steady simulations. For unsteady simulations, forty-eight physical time steps per blade passing period and five pseudo-time iterations are performed each time to obtain converged solutions.

Block-structured grids are generated separately for blade passages and tip clearance by Numeca AutoGrid V5. The rotor passage is meshed in the O4H topology, with a mesh in rotor tip clearance in butterfly topology. H blocks are adopted in the inlet and outlet sections to improve the overall quality of the grid. Grids are clustered near the blade surface and walls to meet the resolution requirement of $y^+ \leq 1$. Three rotor grid systems using the same topology are carried out for the grid-dependency test: Mesh 1 (840,000 nodes), Mesh 2 (1,860,000 nodes), and Mesh 3 (4,570,000 nodes). Considering the computational accuracy and the time consumption,

Mesh 2 was finally used as the rotor grid for subsequent numerical study. A schematic of the main passage and tip clearance grid is shown in Fig. 3.

Eight passage (half-annulus) simulations were conducted to determine the circumferential features of flow instability precisely by taking the last convergence result of the steady simulations as initial conditions. It is considered as near-stall state when the inlet and outlet flow of the calculation domain cannot be kept stable or even perform a significant drop.

2.3 Validation of numerical results

In this section, the numerical method is verified by comparing the experimental results with the numerical results. Figure 4 shows a good match of the circumferentially mass-averaged radial profiles downstream of the rotor. It should be noted that the experimental data are obtained in a single stage at 13.9 kg/s [27, 28], and the numerical data are derived from the simulation of the single rotor at approximately the same
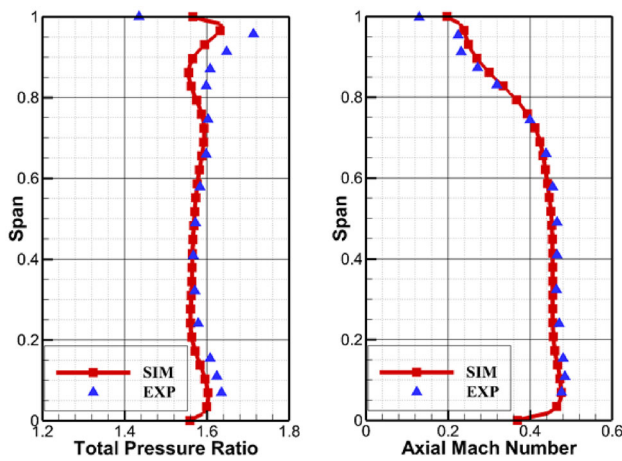
Fig. 4 The comparison of parameters at the rotor exit between simulation and experiment at the near stall condition [27]. (exp:13.9 kg/s; sim: 14.19 kg/s)
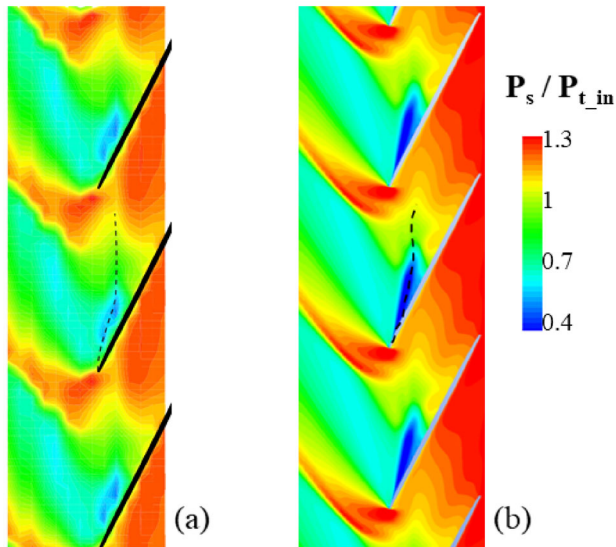

Fig. 5 The pressure distribution of **a** experimental results and **b** unsteady simulation results at the casing wall [28]. (exp:13.9 kg/s; sim: 14.19 kg/s)

mass flow rate. The experimental wall static pressure and the time-average unsteady simulation results at the near stall points are shown in Fig. 5. The trajectory of the tip leakage vortex is marked by the black dashed line indicating the low-pressure trough. The simulation well captures the location and structures of the shock wave.

As illustrated above, the numerical method in this paper can faithfully reflect the critical flow characteristics of the rotor tip at the near-stall situation.
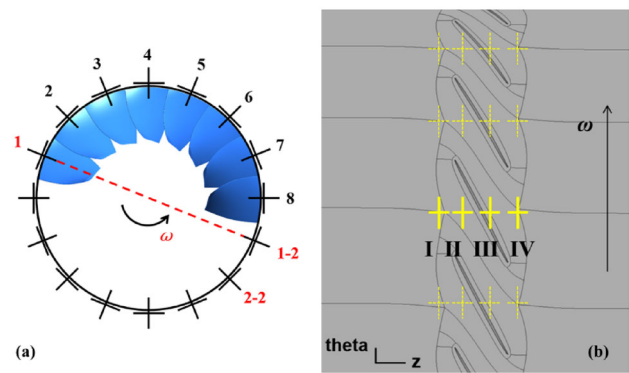
Fig. 6 The diagram of the probes: **a** circumferential direction and **b** axial direction

2.4 Numerical probes

The flow features of the compressor rotor at the near stall condition have an evident trend of circumferential propagation. In order to obtain the pressure signals of the transonic rotor, a set of numerical probes needs to be arranged in the calculation domain. Figure 6 shows a schematic view of the numerical static measurement points near the casing in a stationary frame.

Probes are installed in the stationary frame at 16 circumferential positions to ensure that one probe can capture the pressure signal in each passage regardless of the rotating phase. At each circumferential position, four probes are distributed along the axial direction locating at 25% axial chord length (C_{ax}) upstream the LE, 20% C_{ax} downstream the LE, 70% C_{ax} downstream the LE, and 20% downstream the TE, respectively. The probe numbering was combined by axial position and circumferential position. For example, P_II8 represents the second axial probe at circumferential position 8.

As the computational domain rotates away, the probes outside the domain will fail to acquire a valid pressure signal during a 1/2 T period. At that time, the probe at its symmetrical position will be active and capture the "missing" signals for the full-annulus information. Since the external time step of the eight-passage numerical simulation in this paper is set as 1/48 of a blade-passing-period at 100% rotating speed, about 768 data can be collected in a rotor revolution when the sampling frequency is 256 kHz.

2.5 Wavelet selection

The wavelet transform is a priority for indicating flow characteristics and detecting stall inception on account of its time–frequency ability, which is suitable for analyzing the complicated unsteady signals of axial compressors. For the same time series, different wavelet bases can lead to entirely different spectra. Since the wavelet analysis result is highly
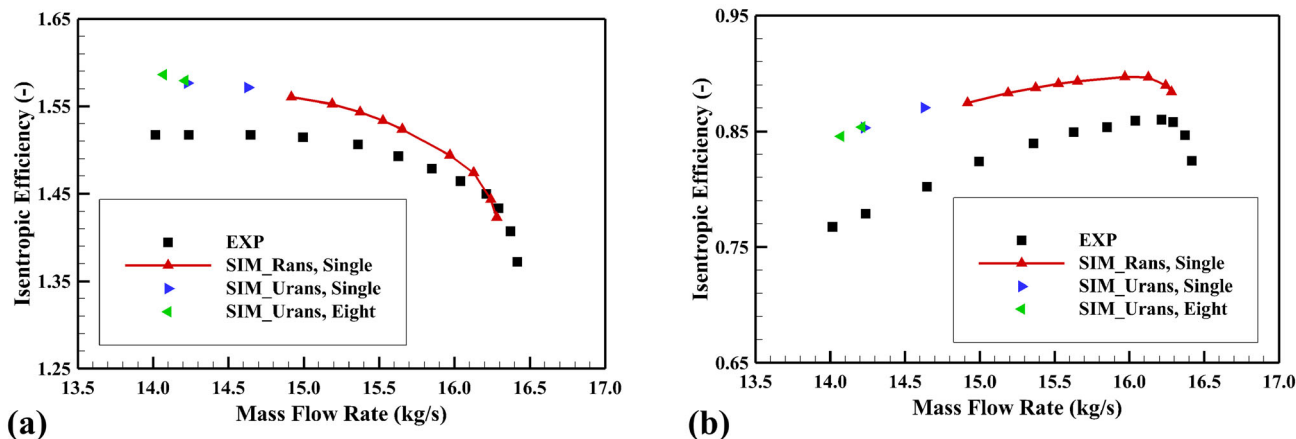
Fig. 7 The compressor performance map: **a** total pressure ratio and **b** isentropic efficiency (EXP: stage exit; SIM: rotor exit)

correlated with the specific value of wavelet basis, in this section, the crucial parameters of the wavelet function will be discussed.

2.5.1 Orthogonal or non-orthogonal

An orthogonal wavelet system, whose *t*-axis might skip the vital instance of the rotation disturbances, is a discrete sequence in both the time and scale domain. In contrast, it is much easier to obtain a smooth and continuous result when applying non-orthogonal wavelets to analyze the pressure signals from rotor-tip flows. Therefore, the latter option will be used to locate the near-stall disturbance and track its development trajectory in this paper. However, it is noteworthy that a spreading phenomenon named energy redundancy would happen in the wavelet spectrum when using non-orthogonal wavelets.

2.5.2 Real or complex

Complex-valued wavelet function is more appropriate than the real-valued for simultaneously capturing the amplitude and phase characteristics. In contrast, the real-valued wavelet function has the highest priority over identifying peaks and singularities. For oscillatory signals, such as rotating disturbances in rotor tip flows, a complex-valued wavelet is preferable to a real-valued wavelet.

2.5.3 Shape and resolution

The Morlet wavelet in the complex domain is chosen with $\omega_0 = 6$ to discuss the near stall behavior in this paper. The expression of the Morlet and its Fourier transform is given in Eqs. (1) and (2), respectively.

$$\psi_0(\eta) = \pi^{-1/4} e^{j\omega_0\eta} e^{-\eta^2/2} \tag{1}$$

$$\psi_0(t) = \frac{(-1)^{m+1}}{\sqrt{\Gamma\left(m + \frac{1}{2}\right)}} \frac{d^m}{dt^m}(e^{-t^2/2}) \tag{2}$$

where ω_0 is the non-dimensional frequency, and *m* is the derivate order. When ω_0 is larger than 5, the Morlet wavelet is regarded to satisfy the admissibility condition. Zhang's study [18] shows that the rotating stall cell fluctuation can be decomposed into the first three-order harmonics with $\omega_0 = 6$.

In this paper, firstly, the non-orthogonal transform is helpful for time series analysis of near stall inception, where smooth, continuous variations in wavelet amplitude are expected. Furthermore, the Morlet wavelet balances time and frequency localization better and contains more oscillations than the DOG wavelet. Besides, the former has been repeatedly verified in engineering projects. Through the above discussion, the Morlet wavelet in the complex domain is chosen with $\omega_0 = 6$ for discussing the unsteady phenomenon of the rotor blade at the NS condition.

3 Results and discussion

3.1 Overall performance

The performance characteristics of total pressure ratio and isentropic efficiency are presented in Fig. 7. In these plots, the hollow squares denote the experimental data measured from a stage environment; the solid curves with triangle-symbols denote the RANS simulation results; the isolated triangles denote the time-averaged results from the URANS simulations. The unsteady simulations are initialized from the last converged point of the single passage steady result. The unsteady simulated points are consistent with experimental data in trend and predict the near stall boundary accurately.
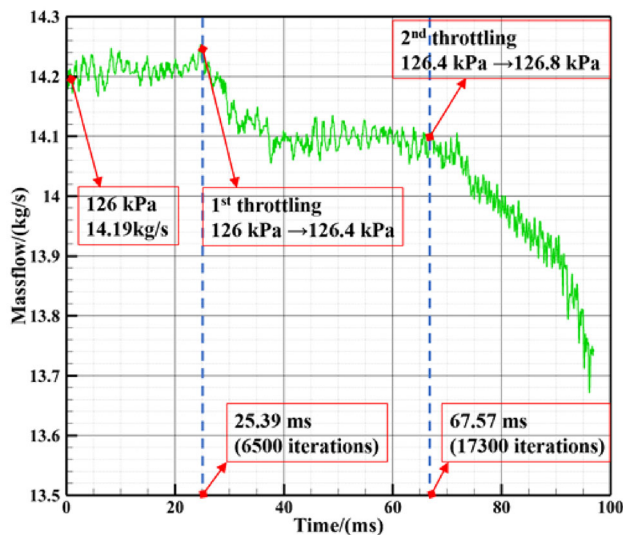
Fig. 8 The history of exit mass flow during throttling towards stall

The prediction of total pressure ratio and isentropic efficiency exhibits a significant over-prediction, ascribed to the expurgation of the downstream stator row. Throttling operation is realized by increasing the back pressure under the minimum flow rate (near stall) condition. The typical throttling process of the eight-passage simulation and corresponding mass flow parameters are exhibited in Fig. 8.

According to the modal proposed by Camp and Day [4], when spike-type oscillations precede the stall, the slope of the overall performance is slightly negative at the near-stall condition. Consequently, it is suggested that spike-type stall inception will occur in the DTC rotor near the stall point.

3.2 Pressure signals

Biela [15] et al. measured the wall pressure signal of the blade tip of the DTC rotor in 2008. They also arranged a set of fast-response probes at about 20% C_{ax} downstream of the rotor LE, which is consistent with the position of the numerical probe row P_II in this paper. Figure 9 (a) shows the Fourier spectra of wall pressure measurement during operation at peak efficiency and near stall, respectively. Besides the rise of overall noise, the increased amplitudes of non-BPF frequencies are clearly visible when the stability limit is approaching, especially the 2–4 kHz band.

The Fast Fourier Transform (FFT) results derived from the P_II probes, located at the identical axial position with the measurement, are shown in Fig. 9 (b). The numerical result accurately exhibits the majority of peak frequencies, 2000 Hz, 3400 Hz and 4600 Hz, for instance. As mentioned above, the numerical simulations are believed to be pretty reliable, considering that various interference factors in the

experiment may cause "noise" in the signal collected by the pressure probes, especially at the near-stall condition.

FFT first processes the original dynamic signal to understand the development of disturbances at different frequencies. Moreover, the spectrum shown in Fig. 10 comes from the high-frequency probes at different axial positions described above. As shown in the spectra, the blade passing frequency (BPF) is recorded dominantly by four axially arranged probes, while the magnitude of this remarkable signal is quite different. The order of BPF-amplitude is above 10^4 at the LE, while a drastic reduction occurred at the TE.

The magnitude of peak amplitude can be regarded as a reflection of the unsteadiness strength. For probe P_I upstream of the LE, the peak amplitudes emerged at approximately 670 Hz and its multiples. The peak amplitudes are distributed in the positions near the domain of 1920 Hz, 3409 Hz, 4668 Hz and 6000 Hz when it comes to P_II. Besides, it is seen that the overall peak amplitudes of the probes arranged at P_III and row IV exhibit a lower intensity comparatively. However, the traditional FFT method does not possess the ability to characterize the oscillation of aerodynamic parameters that arise at the near-stall condition. Following previous experiences, the time–frequency analysis method, for example, wavelet transform, reveals unique advantages when studying the near-stall flow characteristics of the compressor.

3.3 Wavelet analysis results and unsteady disturbance flow characteristics

After the throttling process shown in Fig. 8, we obtained the dynamic pressure at different circumferential positions of the casing. Figure 11 shows the transient pressure signals measured by the numerical probes at each circumferential position of the P_I row during 63–105 ms. It is noted that the amplitude of the signal still exhibits a stable periodic oscillation before 95 ms. However, the third probe caught a slight disturbance at the circumferential position at 98 ms, which does not display a feature of further propagation in the circumferential direction. Then a much remarkable large-scale disturbance appeared at the position of downstream probe P_I4, corresponding to the velocity of development at 60% rotation speed. Afterward, the amplitude of the disturbance further expanded and developed into stall inception.

In Fig. 12, the wavelet transform is applied to the data of pressure probe P_I1. It can be seen that there are two evident energy discontinuities in the amplitude band of BPF (area near 5333 Hz), with a distinct spreading phenomenon corresponding to the location of the horizontal axis at 100.8 ms and 103.4 ms. The energy discontinuity mentioned above caused a visible amplitude increase in the frequency domain during 1000–4000 Hz, which is consistent with the wavelet analysis
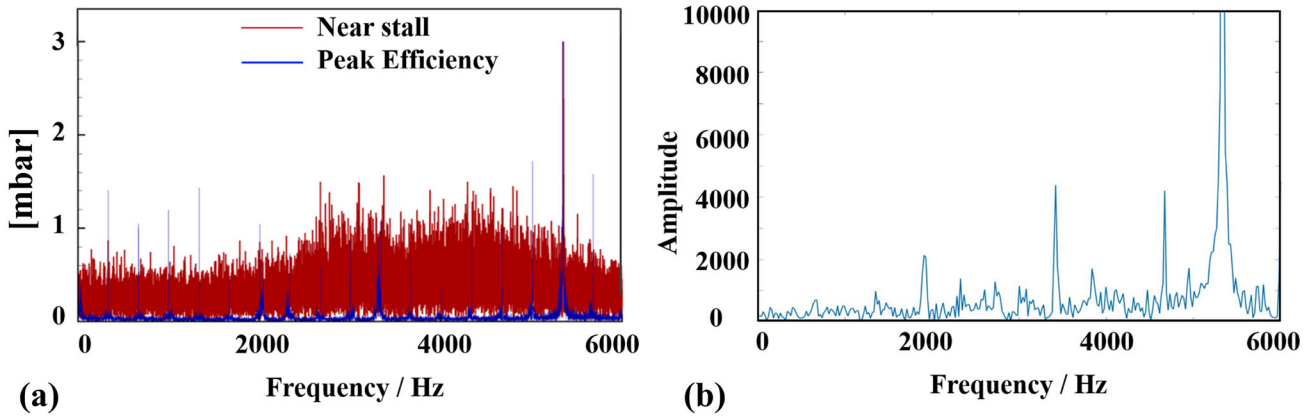
(a)   **(b)**

Fig. 9 The Fourier spectra of **a** experiment [15] and **b** simulation at the near stall condition

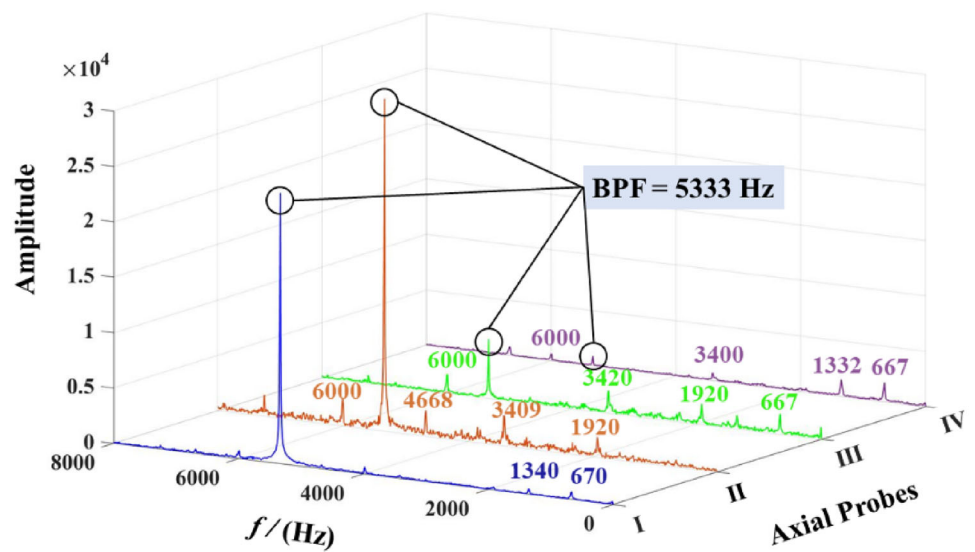**Fig. 10** The Fourier spectra of casing pressure signal at different axial positions

Fig. 11 Pressure signal at different circumferential positions during 65–105 ms
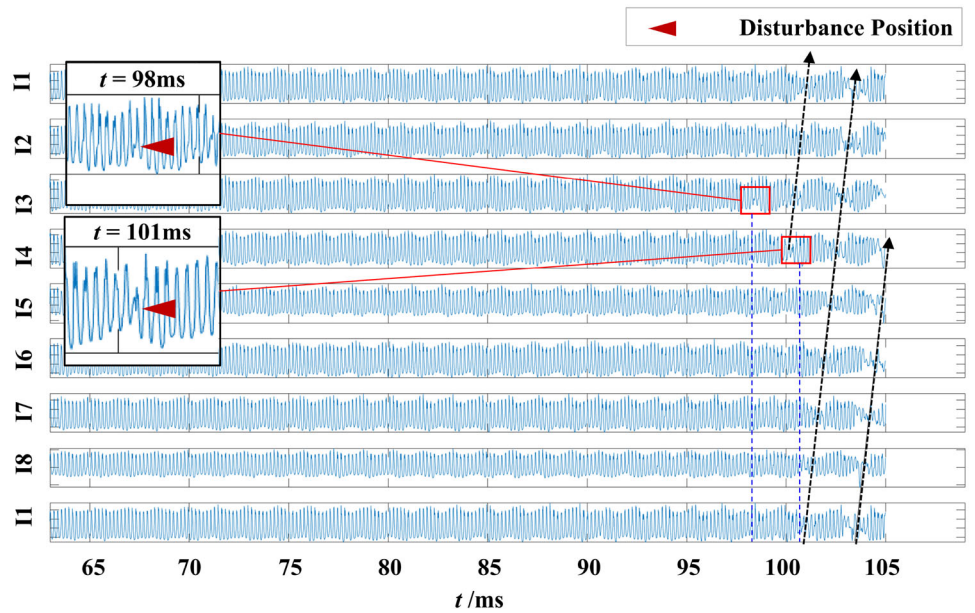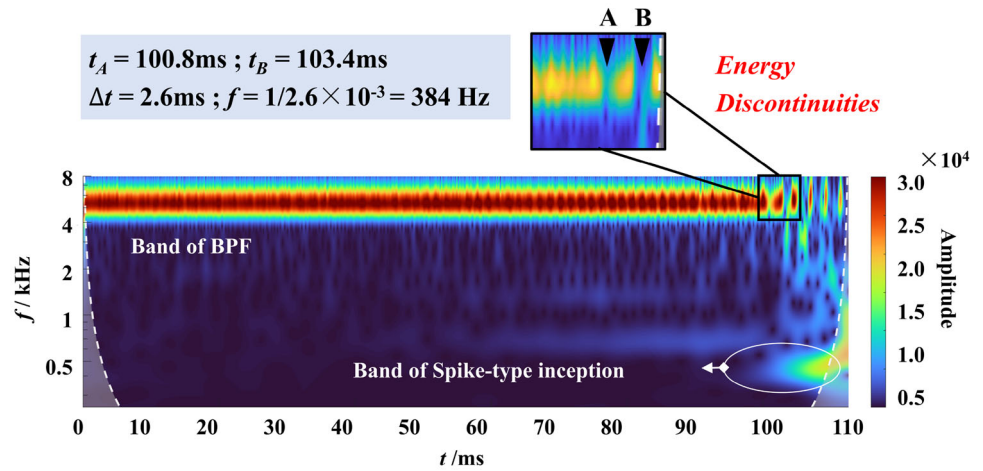
Fig. 12 The wavelet spectrum of pressure signal at P_I1 during 0–110 ms

results of the wall pressure signals from another low-speed compressor [17].

In addition, a maximum amplitude region in the frequency domain is generated starting from 96 ms in the spectrum, located at a frequency band of 300–500 Hz. It is noted that the time interval between the energy discontinuity of BPF is approximately 2.6 ms, during which the disturbance is required to pass through the eight passages completely, with a converting frequency of 384 Hz. From the findings above, it is reasonable to propose that the spike-type inception with the feature of circumferential propagation was captured by probe P_I1 at certain moments.

In Fig. 13, the bands of BPF in the wavelet spectra for all eight probes of P_I are placed in line for the same period. The result of P_I1 is repeated at the bottom to illustrate the cyclic placement of numerical probes. By comparing the trajectory of the spike-type distribution, we can clearly see that the rotating asymmetry is even conspicuous in the flow field at the rotor tip region, as indicated by the black dashed arrow. The spikes travel circumferentially at about 60% rotating speed. The frequency and modal analyses reveal the temporal and spatial features of the rotating instability. Then, the associated unsteady flow characteristics in the rotor tip region are displayed.

As shown in Fig. 14, the static pressure distribution at 98% span is presented every 1/4 T from 101.25 ms (denoted as t_1). Since these disturbances are constantly generated, propagated, and disappeared periodically, only the results within one period are displayed. At $t = t_1$ and $t = t_1 + 1/4$ T, the structure of leakage flow in the passage between B4 and B5 has been destroyed. Meanwhile, the rotational asymmetry of each passage of the tip region is further aggravated. The shock wave structure and static pressure rise are significantly affected as well.

At $t = t_1 + 2/4$ T, a new structure consistent with all the flow characteristics of the upstream option is generated in the passage between B5 and B6. Besides, the two distinct

low-pressure spots, marked as M and N, have been located upstream of the LE of the B6. Similarly, the low-pressure regions with a broader range and higher intensity also exist in other circumferential passages. This means a new low-pressure region has been formed in the SS of the blade with the extinction of the former low-pressure area, while the spots in the middle repeat their previous behavior.

Therefore, it is believed that an apparent circumferential propagation phenomenon against the rotating direction appears in the tip flow region after $t_1 + 1/4$ T, which takes approximately 1/4 T to pass through the single rotor passage in the relative frame. According to the Nyquist Sampling Theorem, the time scale of a full-annulus propagation of the distribution collected by stationary probes is 2/3 T, with a converting frequency of 500 Hz. It is close to the frequency of the spike-type stall inception in the wavelet analysis. It can be concluded that the disturbance captured by numerical probe P_I1 is identified evidently as a physical vision of spike inception.

3.4 Stall mechanism of the rotor tip

3.4.1 Blade loading

The development of the low-pressure spots has a distinct effect on the tip loading, closely related to the stall behavior. Figure 15 shows the blade loading perturbation caused by SS separation in the tip region at four instants from 86.39 ms (denoted as t_2). The pressure coefficient C_p is defined as:

$$C_p = \frac{p_s - p_{s,in}}{\frac{1}{2}\rho U_m^2} \qquad (3)$$

where p_s is the local static pressure, and $p_{s,in}$ is the average static pressure at the inlet plane, U_m is the tangential velocity at mid-span.

Fig. 13 Wavelet spectrum of pressure signal at different circumferential positions
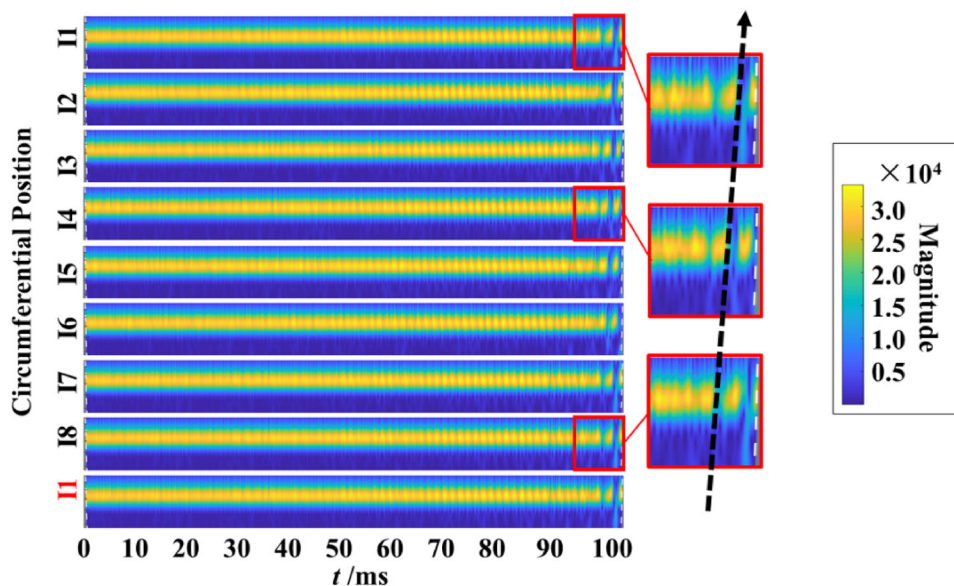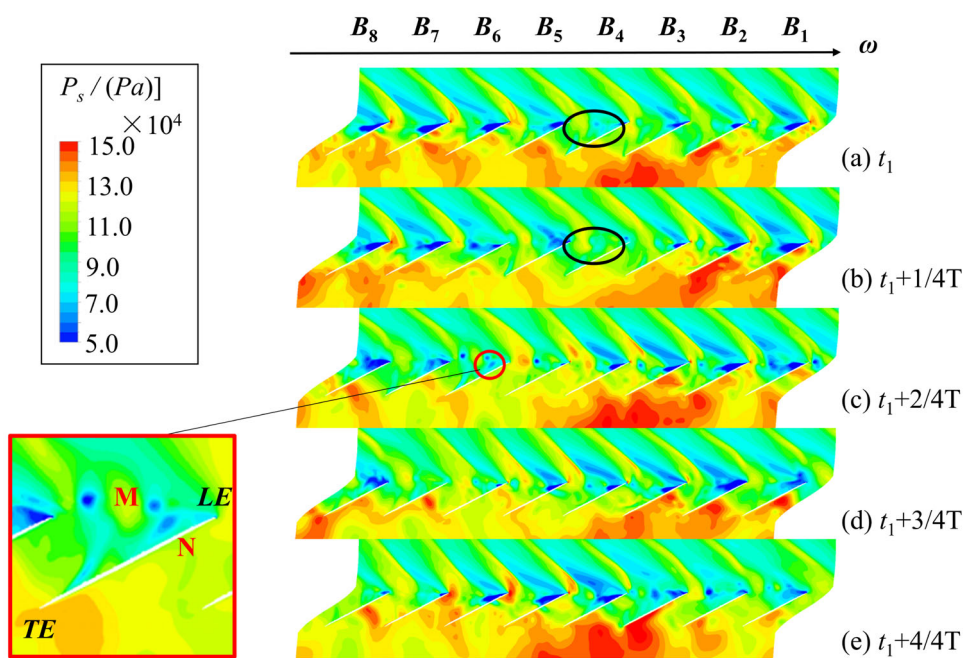

Fig. 14 Pressure distribution at 98% span at different moments

As seen in Fig. 15 (a), a low-pressure spot generated by the shedding of a leaking vortex causes a significant drop when it moves to the LE of the PS. Then, a secondary leakage occurs, sliding through the tip clearance, and leads to a specific increase of static pressure at the corresponding position. At $t = t_2 + 10/128\ T$, the low-pressure spot has moved downstream with a conspicuous intensity reduction. Notably, a new low-pressure region has been formed in the SS of the blade with the extinction of the former spot, while the low-pressure region in the middle just repeats its previous behavior. In addition, the pressure contours on the blade to the blade surface at two corresponding moments are proposed in

Fig. 16 to dedicate the specific flow mechanism behind the blade loading changes.

Some characteristics of the shock wave in the passage can also be observed from the loading distribution map. In general, the shock wave is located near the 40% C_{ax} of the SS, and there are inevitable fluctuations in this vicinity. At the moment of Fig. 15 (a), the shock wave is roughly located at the position of 25–40% C_{ax}, and in Fig. 15 (b), the static pressure increases due to the shock wave occurring at 30–50% C_{ax} position.

Fig. 15 Blade loading distribution at 98% span in different instants: **a** $t_2 + 4/128$ T, **b** $t_2 + 7/128$ T, **c** $t_2 + 10/128$ T and **d** $t_2 + 13/128$ T
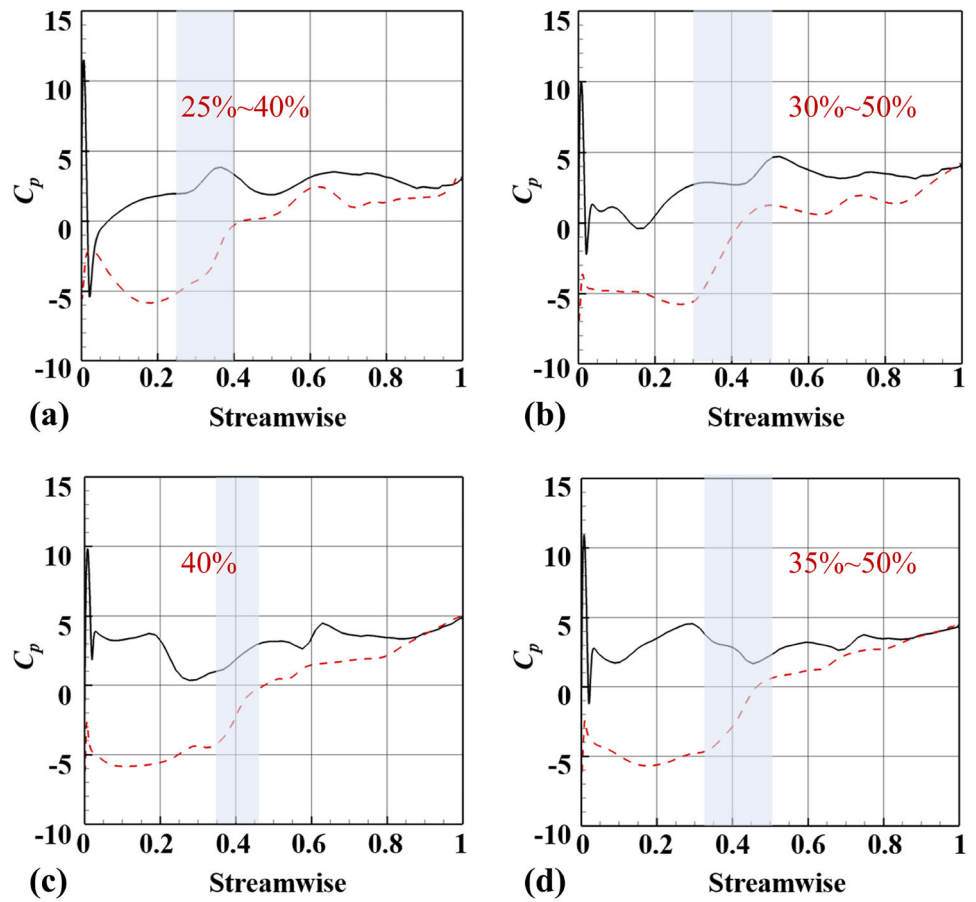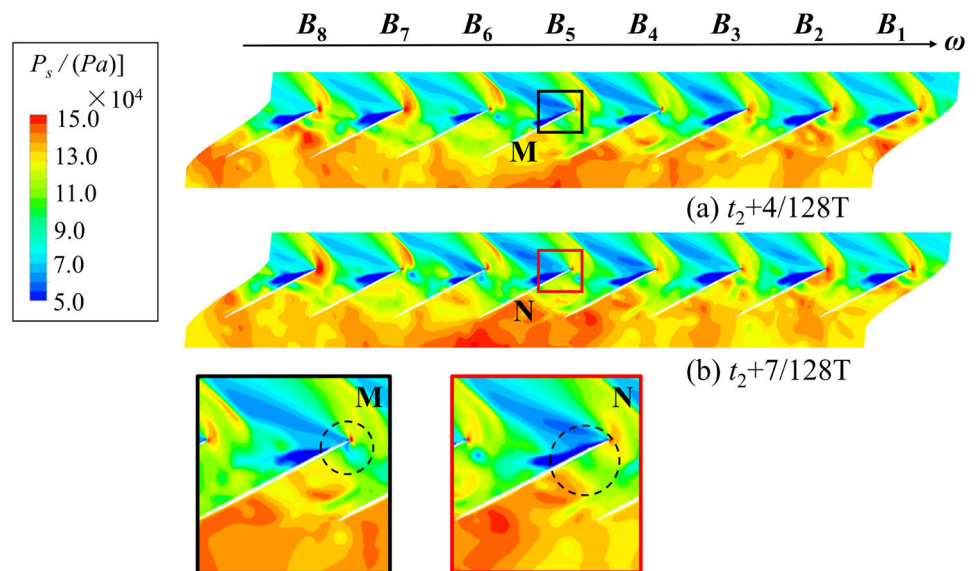

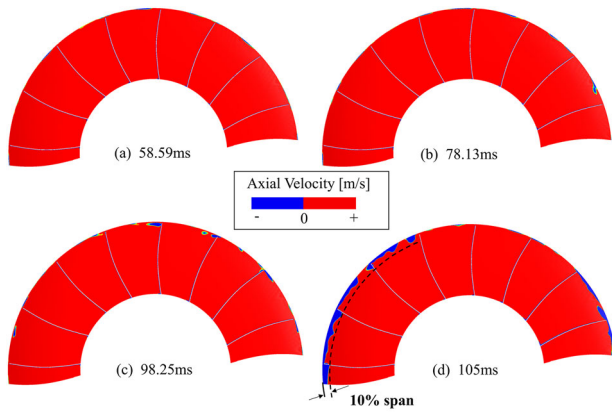**Fig. 16** Pressure distribution at 98% span at different moments

Fig. 17 The axial velocity distributions at the LE plane at different times

3.4.2 Spillage and backflow

The two necessary conditions for forming spike inception proposed by Vo [6], leading edge spillage and trailing backflow, have been verified by researchers in experimental and numerical methods. These flow behaviors are also observed in the flow field of our simulation results. Figure 17 shows the axial velocity distribution from the upstream perspective of the rotor LE, in which the positive axial velocity area is marked in red. In contrast, the negative region is marked in blue. It is apparent that the spillage region at the LE gradually increases with the development of the tip clearance flow. The blockage caused by the flow behaviors occupies more than 10% of the passages at 105 ms, with the pressure signals of stall inception captured in the meantime.
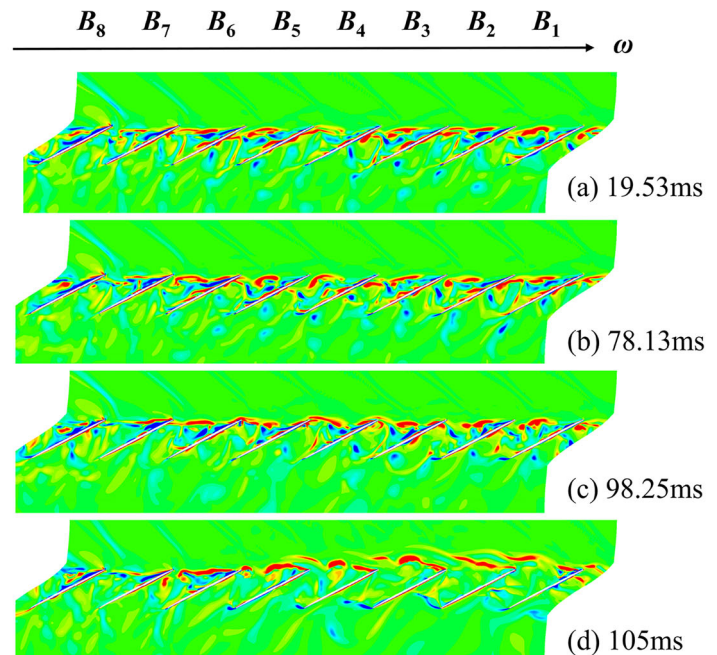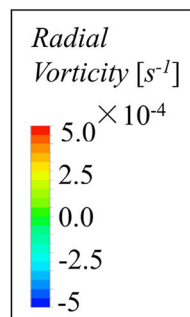
It is credible from the previous study that the leading edge spillage is mainly affected by the tip leakage flow. In order to depict the flow details and capture the instability sources at the tip region of the blade, a series of contour plots about instantaneous vorticity at 98% span is shown in Fig. 18. The leakage flow in each passage has developed to a particular position and almost flushes with the LE plane of the rotor tip from 19.53 to 78.13 ms. Moreover, the structure of the tip leakage vortex was intact as the blockage further increased. Then, a perturbation in the local flow coefficient causes the tip leakage flow to move upstream, spilling forwards of the LE at 98.25 ms. This spillage interacts with the adjacent tip leakage flow and develops into a circumferentially propagating vortical structure, which triggers a leading edge separation on B1 to B3 at 105 ms. Simultaneously, spike-type stall inception is generated in the corresponding passage, as shown in Fig. 18 (d).

Figure 19 shows relative velocity vectors at 98% span with streamlines at the near stall condition, with the regions of interest marked with circles. There is no conspicuous trailing backflow in all rotor passages in the initial time ($t3 = 98.25$ ms). As shown in Fig. 19(b–d), various degrees of trailing backflow occurred in some passages successively. Since the axial velocity value of the corresponding position is not high enough, it is unable to make many contributions to the blockage, mainly located at the mid-upstream area in passages. As seen in Fig. 19 (e), an intense trailing backflow emerged in the passage between B2 and B3, which propagates upstream after passing through blade B2, and finally reaches the SS of the adjacent rotor. At this moment, the axial velocity has reached approximately − 120 m/s. The intense

Fig. 18 Radial vorticity at 98% span

Fig. 19 The velocity distribution and axial velocity distribution at 98% span during 99–105 ms

Fig. 20 Tip separation phenomena at 102 ms: **a** Q-criterion and **b** Pressure distribution

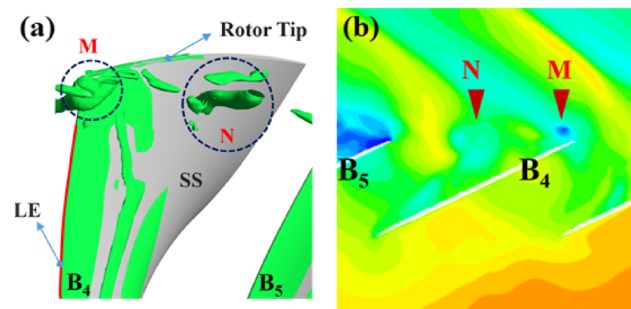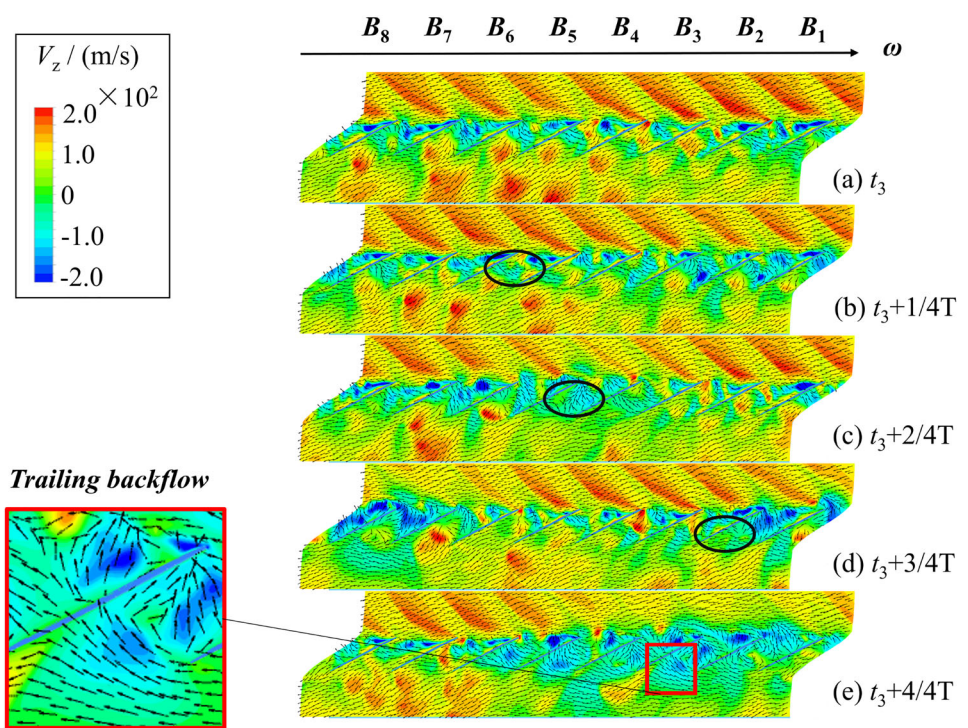**Fig. 21** Tip separation phenomena at 105 ms: **a** Q-criterion and **b** Streamline

backflow caused a further blockage in the passage, with obvious stall inception already indicated in the flow field.

3.4.3 Tip separation

Figure 20 shows the vortex structure in the blade tip region with the Q criterion at 102 ms instant to visualize the three-dimensional evolution and the different influences of the leakage vortex after overflowing the LE. The blockage causes a large enough incidence increase onto the tip region of the blade to trigger the LE separation, creating a radial vortex, the spike, which propagates in the passages and grows in size, and provides positive feedback for further separation.

At 105 ms instant, a more obvious vortex structure appeared in the passage, as indicated by the blue dashed line in Fig. 21 (a), which starts from the midstream of the
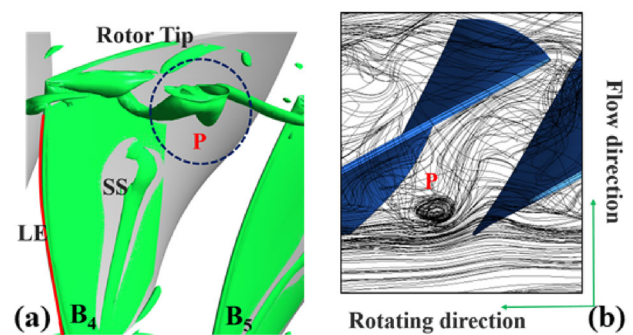
SS of the blade and terminates at the casing with a vertical state. It is notable from the streamlines that this transverse vortex has moved circumferentially more than a half-passage length. Besides, the conclusion will be drawn adequately that the distinct increase of vorticity between blade B4 and B5 as seen in Fig. 18 (d) was caused by the radial "tornado-type" vortex as seen in Fig. 21 (b).

4 Conclusion

Unsteady simulations are conducted for the DTC transonic rotor to investigate the specific characteristic and propagating mechanisms of spike-type stall inception. The wavelet

analysis method based on the static pressure signals is combined with specific flow fields to reveal the generation and development of the stall inception. Several conclusions are drawn below:

(1) The unsteady CFD method in this paper favorably depicts the overall performance characteristics. It shows a good match of the radial profiles between experimental data and numerical results at the near-stall condition. The unsteady flow behaviors at the rotor tip region are well depicted. The numerical methodology adopted in this paper can accurately simulate the operating process from near-stall throttling to rotating instability. The setting layout of the probes is quite reasonable, which can effectively capture the dynamic pressure at the rotor tip over the circumferential range.

(2) Wavelet transform with a suitable function base is a natural choice for investigating pre-stall disturbances and detecting stall inceptions. By comparing the spectra of the FFT and time–frequency analysis results, the disturbance captured by the numerical probe located at 25% axial chord length upstream of the LE during the period from 100.8 to 103.4 ms is confirmed as a typical spike-type stall inception. The spikes travel circumferentially at about 60% rotating speed. The characteristic frequencies also correspond to other temporal and spatial features of the rotating instability, such as the fluctuation of the shock wave, self-oscillation, and propagation of tip leakage vortex.

(3) Spike-type disturbances correspond to the moving areas of low pressure essentially, which are caused by flow separation and radial vortex formation. The unsteadiness reflected on the wavelet spectrum and flow field at the tip region of the blade is dominated by the evolution of radial vortex structure inside the rotor passage, which triggers a tip clearance spillage flow and a trailing backflow.

Declarations

Conflict of interest The authors declare no conflict of interest.

References

1. Day IJ (1991) Stall inception in axial flow compressors. J Turbomach 115(1):1–9
2. Moore FK, Greitzer EM (1986) A theory of post-stall transients in axial compression systems: part I—development of equations. J Eng Gas Turbines Power 108(1):68–76
3. Jackson AD (1987) Stall cell development in an axial compressor. J Turbomach 109(4):492–498
4. Mcdougall NM, Cumpsty NA, Hynes TP (1990) Stall inception in axial compressors. J Turbomach 112(1):116–123
5. Camp TR, Day IJ (1997) A study of spike and modal stall phenomena in a low-speed axial compressor. J Turbomach 120(3):393–401
6. Vo HD, Tan CS, Greitzer EM (2008) Criteria for spike initiated rotating stall. J Turbomach 130(1):011023
7. Pullan G, Young A, Day I et al (2015) Origins and structure of spike-type rotating stall. J Turbomach 137(5):051007
8. Inoue M, Kuroumaru M, Tanino T et al (2001) Comparative studies on short and long length-scale stall cell propagating in an axial compressor rotor. J Turbomach 123(1):24–30
9. Yamada K, Kikuta H, Iwakiri K-I et al (2013) An explanation for flow features of spike-type stall inception in an axial compressor rotor. J Turbomach 135(2):021023
10. Hewkin-Smith M, Pullan G, Grimshaw S et al (2019) The role of tip leakage flow in spike-type rotating stall inception. J Turbomach 141(6):061010
11. Kim S, Pullan G, Hall C et al (2019) stall inception in low-pressure ratio fans. J Turbomach 141(7):071005
12. Cameron JD, Morris SC (2013) Analysis of axial compressor stall inception using unsteady casing pressure measurements. J Turbomach 135(2):021036
13. Tryfonidis M, Etchevers O, Paduano J et al (1994) Pre-stall behavior of several high-speed compressors. J Turbomach 117(1):62–81
14. Li C, Xu S, Hu Z (2015) Experimental study of surge and rotating stall occurring in high-speed multistage axial compressor. Proced Eng 99:1548–1560
15. Biela C, Müller MW, Schiffer H-P, et al. 2008, "Unsteady pressure measurement in a single stage axial transonic compressor near the stability limit". ASME Turbo Expo 2008: GT2008–50245.
16. Grossmann A, Morlet J (1984) Decomposition of Hardy functions into square integrable wavelets of constant shape. SIAM J Math Anal 15(4):723–736
17. Lin F, Chen J, Li M (2004) Wavelet analysis of rotor-tip disturbances in an axial-flow compressor. J Propul Power 20(2):319–334
18. Zhang H, Yu X, Liu B et al (2016) Using wavelets to study spike-type compressor rotating stall inception. Aerosp Sci Technol 58:467–479
19. Liu Y, Li J, Du J et al (2019) Application of fast wavelet analysis on early stall warning in axial compressors. J Therm Sci 28(5):837–849
20. Huang NE, Long SR, Shen Z (1996) The mechanism for frequency downshift in nonlinear wave evolution. Adv Appl Mech 32(1):59–117
21. Li CZ, Xiong B, 2011, "Application of HHT for Aerodynamic Instability Signal Analysis in Compressor", Proceedings of 2011

3rd International Conference on Signal Processing Systems (ICSPS 2011), pp. 43–47.

22. Park HG., 1994, "Unsteady disturbance structures in axial flow compressor stall inception", Massachusetts Institute of Technology thesis.

23. Lin P, Wang M, Wang C et al (2019) Abrupt stall detection for axial compressors with non-uniform inflow via deterministic learning. Neurocomputing 338:163–171

24. Danner FC, Kau H-P, Müller MM, et al. 2009, "Experimental and numerical analysis of axial skewed slot casing treatments for a transonic compressor stage", ASME Turbo Expo 2009: GT2009–59647

25. Menter FR, Kuntz M, Langtry R (2003) Ten years of industrial experience with the SST turbulence model. Turbul Heat Mass Transf 4(1):625–632

26. Wilke I, Kau H P., 2002, "A Numerical Investigation of the Influence of Casing Treatments on the Tip Leakage Flow in a HPC Front Stage", ASME Turbo Expo 2002: GT2002–30642.

27. Müller M, Schiffer H-P, Voges M, et al., 2011, "Investigation of passage flow features in a transonic compressor rotor with casing treatments", ASME Turbo Expo 2011: GT2011–45364.

28. Müller MW, Biela C, Schiffer H-P, et al, 2008. "Interaction of rotor and casing treatment flow in an axial single-stage transonic compressor with circumferential grooves", ASME Turbo Expo 2008: GT2008–50135.

29. Xia KL, Feng JD, Zhu MM, et l., 2022, "Numerical research on near stall characteristics of a transonic axial compressor based on wavelet analysis", ASME Turbo Expo 2022: GT2022–82366.